ORIGINAL ARTICLE

Investigating the Foaming Process of a Thermoplastic Elastomer (TPE) Using Rheology and Image Analysis

Hyo Jae Kong[1] · Hyeong Yong Song[2] · Seung Hak Lee[3] · Sumkun Lee[4] · Gyungbok Kim[1] · Nakyong Yun[1] · Kyu Hyun[4]

Abstract

This study introduced a method to simultaneously characterize time-resolved rheological and volumetric changes occurring during the foaming process of a thermoplastic elastomer containing an encapsulated physical blowing agent. For this, a conventional rotational rheometer was equipped with a commercial digital camera to capture video recordings. These video recordings were digitized into volumetric data using custom-written computer-vision-based algorithm. We first investigated rheological and volumetric changes during temperature ramp tests. The calculated cell volume fractions varied quantitatively depending on cell expansion and shrinkage. The viscoelastic moduli followed the characteristic behavior of the cell volume fraction. Furthermore, to analyze the volumetric changes under hypothetical processing conditions, a four-stage protocol comprising time sweep and temperature ramp was designed. The results revealed that the cell shrinkage induced by internal gas permeation at high temperatures was significantly greater than that induced by internal pressure reduction during cooling. Finally, comparison between foam densities computed using our algorithm and those measured using a densimeter revealed good agreement within 3% relative error. This demonstrates the applicability of our algorithm for quantitatively assessing volumetric changes of foam.

Introduction

Foams are well-dispersed bubbles or gaseous voids inside a dense matrix. In polymer foams, which comprise two phases, blowing agents are commonly used to create void structures within polymer. The foaming science and technology have been developed for many years and have been applied to

Hyo Jae Kong and Hyeong Yong Song have contributed equally.

✉ Kyu Hyun
kyuhyun@pusan.ac.kr

[1] Material Research and Engineering Center, AVP Division, Hyundai Motor Company, Uiwang-si 16082, South Korea

[2] Institute of Chemical Technology and Polymer Chemistry, Karlsruhe Institute of Technology, 76131 Karlsruhe, Germany

[3] AMR Equipment Development Team, Samsung SDI, Yongin-si 17084, South Korea

[4] School of Chemical Engineering, Pusan National University, Busan 46241, South Korea

different types of polymers [1, 2]. Polyolefin foams, notable types of polymer foams, offer several advantages over unfoamed polymers, including higher specific strength, better thermal insulation, low density, and lightness. Consequently, since their introduction in the early 1960s, polyolefin foams have found widespread applications across numerous manufacturing sectors including sports equipment, toys, insulation, automotive, buoyancy, and cushioning [3, 4]. More recently, the application of polyolefin foams has expanded to three-dimensional (3D) printing to meet industrial needs [5–7].

Generally, most polymer foams are manufactured by dispersing a gas phase using blowing agents. The blowing agents are broadly classified as physical blowing agents (PBAs) and chemical blowing agents (CBAs) based on their mechanism [3]. CBAs generate gas through chemical reactions or thermal decomposition under foaming conditions, while PBAs release gas through changes in their physical states during foaming.

One of the noticeable PBAs is an encapsulated PBA. It contains a low-boiling-point liquid hydrocarbon

encapsulated within a thermo-expandable acrylonitrile copolymer shell. With increasing temperatures, the copolymer shell softens, allowing the gasification of the encapsulated hydrocarbon. Finally, the shell expands under increased internal pressure, creating micro-balloons. Notably, during the foaming process, the acrylonitrile copolymer shell softens without melting, thus preventing the coalescence of the expanded shells. These characteristics allow encapsulated PBAs to create controlled and uniform cell structures, independent of external pressure conditions [8, 9]. However, at temperatures beyond a critical point, gasified hydrocarbons can permeate through the thin copolymer shell, causing a decrease in internal pressure and subsequent shrinkage of the encapsulated PBAs. Consequently, the thermo-mechanical behavior of polymer foams containing encapsulated PBAs plays a key role in the foaming process.

Another key factor is the viscoelasticity of polymer foam. The viscoelastic properties influence the foaming mechanism at various stages, including bubble nucleation, cell growth, stabilization, and shrinkage [5]. Rheological measurements provide viable tools for characterizing both the thermo-mechanical and viscoelastic properties of polymer foams. Although many studies have employed rheological measurements to correlate the viscoelastic properties of unfoamed matrix with the final characteristics of foams (cell size, cell density, and volume expansion ratio) [10–13], only a few have examined the rheological changes involved in the foaming process. Lee et al. [9] reported that the dispersion of an encapsulated PBA within epoxy resin led to the development of a positive axial force due to cell expansion. From this point, our previous study investigated the foaming process of a polyolefin elastomer (POE) containing a CBA or an encapsulated PBA by simultaneously tracking the shear modulus and axial normal force [8]. The results revealed that regardless of the type of blowing agents used, the axial normal force increased rapidly at the activation temperature of the blowing agents. The observed peak in the axial normal force correlated with characteristic changes in shear modulus development.

Going one step further, we propose an approach involving simultaneous evaluations of the rheological properties and volumetric changes of polymer foams. From an industrial perspective, monitoring the volumetric changes of foams is crucial. For instance, foam soles for footwear are produced through multi-compression molding as one-step molding is not enough to achieve the required foam dimensions [8, 9]. In addition, in foam 3D printing, controlling the final shapes and dimensions of products is essential to prevent over-expansion or distortion [5–7]. To accurately quantify foam volumetric changes during foaming, we integrate image analysis with computer vision technique. Computer vision is a branch of computer science that enables computers to interpret object information from images and videos [14].

Recently, a quantitative volumetric characterization method has been developed using image analysis based on computer vision and has become an important tool in engineering and medical fields [15–20].

In this study, we aimed to simultaneously measure the rheological properties and volumetric changes of a thermoplastic elastomer (TPE) undergoing foaming in the presence of an encapsulated PBA. To this end, a conventional rheometer was combined with a digital camera to record footage of the volumetric changes in the foam. The rheometer monitored the thermal expansion and shrinkage of the TPE foam as functions of temperature and time. Concurrently, the whole experimental process was captured by the digital camera, and the volumetric changes in the TPE foam were analyzed using an image analysis method based on the computer vision technique.

Experimental Section

Materials

Due to its excellent toughness, flexibility, and ease of processing, ethylene-octene copolymer (EOC) was used as the thermoplastic elastomer (TPE) in our study. The EOC (ENGAGE™ 8137 grade, melt flow index = 13 g/10 min at 190 °C/2.16 kg) was supplied by Dow Chemicals (Midland, MI, USA). The encapsulated PBA (FN-105 grade) was provided by Matsumoto Yushi-Seiyaku Corporation (Japan). The average capsule size and shell thickness of FN-105 were 35–45 µm and 2–15 µm, respectively. Based on details provided by the supplier, the expansion start temperature of FN-105 was 120–135 °C and the maximum expansion temperature was 175–185 °C. Furthermore, we incorporated dicumyl peroxide (DCP) (AkzoNobel, the Netherlands) as a curing agent within the EOC matrix. The DCP helped stabilize bubbles during the expansion and subsequent shrinkage of the foam [1], facilitating more explicit measurements of volumetric changes at the cell shrinkage stage by hindering rapid hydrocarbon gas permeation. Furthermore, a foam promoter (zinc oxide, ZnO), processing aid (stearic acid, St/a), pigment (titanium dioxide, TiO_2), and crosslinking coagent (triallyl cyanurate, TAC) were used as other additives.

Sample Preparation

To prepare the EOC/PBA compounds, the encapsulated PBA was mixed with the EOC, DCP, and other additives (ZnO, St/a, TiO_2, and TAC) in two stages. First, EOC pellets, ZnO, St/a, TiO_2, and PBA were placed in an internal mixer (Daesung Tester, South Korea) and melted for 10 min. Subsequently, DCP and TAC were added and

Table 1 Nomenclature and compositions of ECP/PBA compounds with different PBA concentrations

Nomenclature	Composition [phr]						
	EOC	DCP	TAC	ZnO	St/a	TiO$_2$	PBA
ECP	100	1.5	0.2	2.5	2.0	5.0	0
ECP/PBA2							2
ECP/PBA4							4
ECP/PBA6							6
ECP/PBA8							8

mixed at 80 °C under a rotor speed of 40 rpm for 5 min. In total, four different concentrations of the PBA [2, 4, 6, and 8 in parts per hundred (phr)] were selected for the evaluation. For simplicity, EOC containing DCP and the other additives were referred to as ECP. Table 1 lists the compositions and nomenclature of all compounds.

Rheological Measurements

The rheological properties of the series of ECP/PBA compounds were measured using a strain-controlled rheometer (ARES-G2, TA Instruments, USA) equipped with a parallel-plate geometry. A plate with a diameter of 8 mm was selected to prevent dramatic torque increments during curing and foaming. The measurement temperature was controlled by a forced convection oven (FCO).

First, temperature ramp tests were conducted in the range of 100–190 °C (heating rate = 3 °C/min) to investigate the temperature dependence of the ECP/PBA compounds. The applied strain amplitude (γ_0) and angular frequency (ω) were 0.02 and 1 rad/s, respectively. In addition, the axial force adjustment option was activated. By doing so, the normal force transducer detected any change in the axial normal force during curing, foam expansion, and shrinkage. As a result, the gap between the two plates was adjusted automatically to maintain a constant axial normal force.

Subsequently, we designed a rheological measurement protocol to describe time-resolved changes that might be observed during an actual foaming process. Figure 1 depicts the applied temperature profile. In the first stage, time sweep tests were performed at 100 °C for 1 min within the linear viscoelastic regime ($\gamma_0 = 0.1$ and $\omega = 1$ rad/s). Then, the temperature was increased rapidly from 100 to 170 °C at a heating rate of 60 °C/min. In the third stage, time sweep tests were conducted at 170 °C for 10 min within the linear viscoelastic regime ($\gamma_0 = 0.01$ and $\omega = 1$ rad/s). In the fourth stage, the temperature cooled down from 170 to 45 °C at a cooling rate of 10 °C/min. The applied γ_0 and ω were 0.002 and 1 rad/s, respectively.
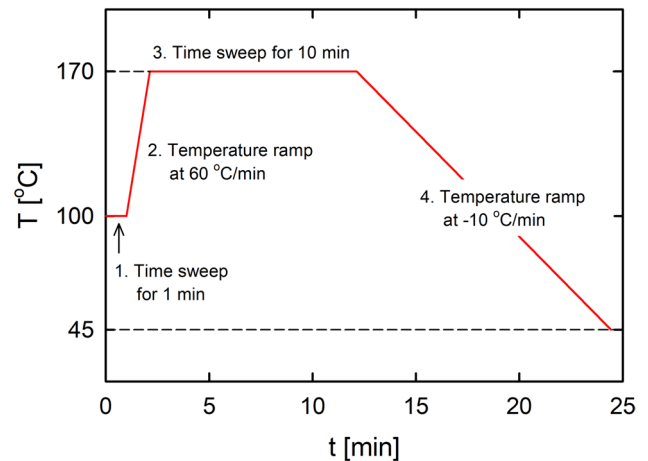

Fig. 1 Time (t)–temperature (T) profile to mimic a hypothetical foaming process sequence
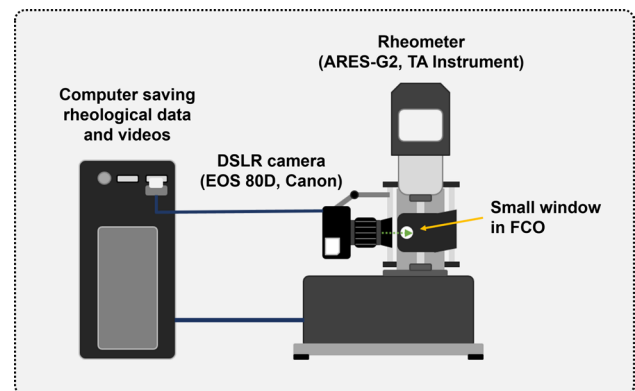

Fig. 2 Schematic of the setup for the computer vision system

In all the stages, the axial force adjustment remained active.

Setup of the Computer Vision System

Figure 2 depicts a schematic of the computer vision system setup. For computer-vision-based image analysis, a commercial digital single lens reflex (DSLR) camera (EOS 80D, Canon, Japan) was mounted onto the ARES-G2 rheometer.

The lens specification was EF-S 18–55 mm f/3.5–5.6 IS STM. During rheological measurements, a full high-definition (HD) video was recorded at 25 frames/s through the glass window of the forced convection oven (FCO).

The image processing and analysis of the recorded video were performed using a custom-written MATLAB code. A detailed description of the image processing is presented in the next section.
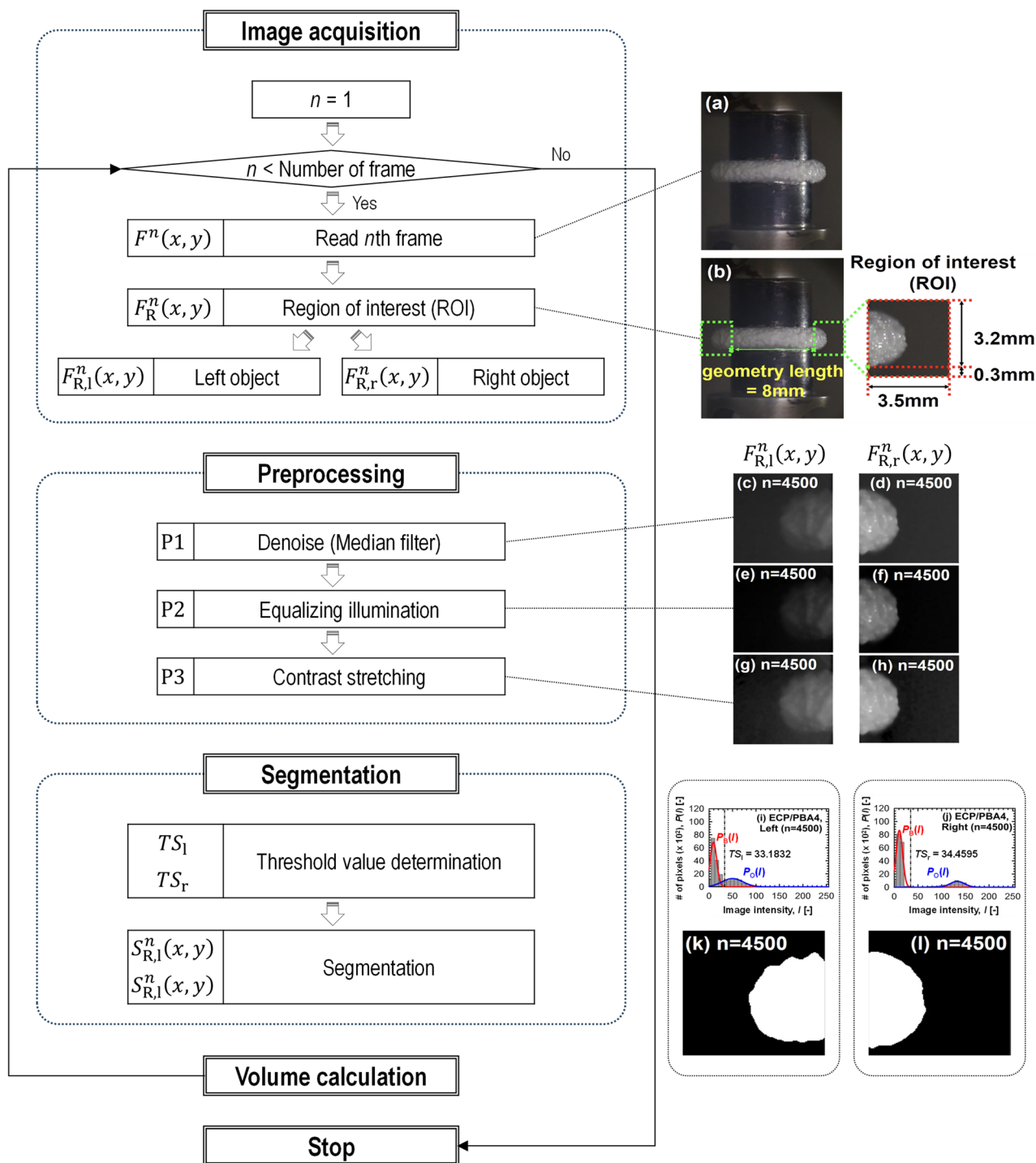

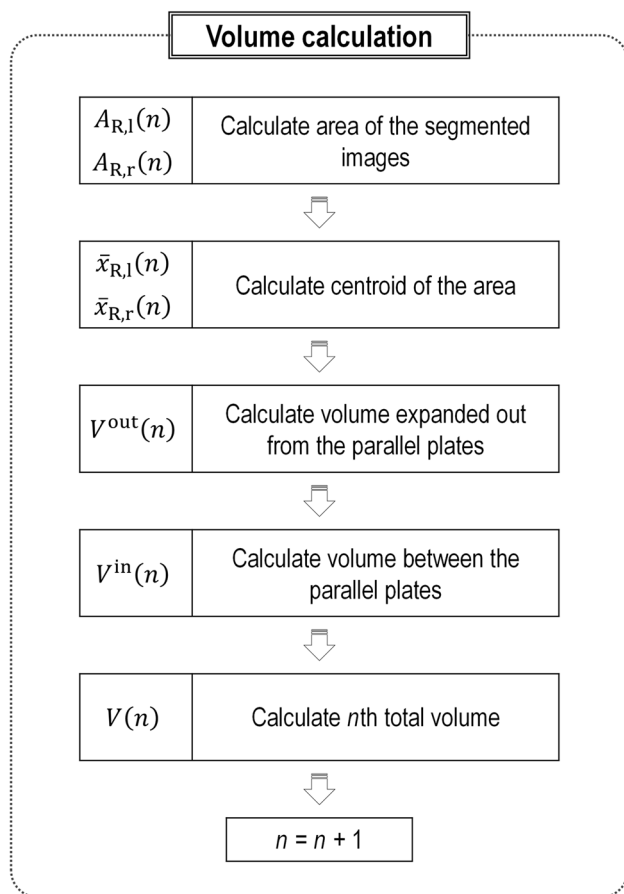**Fig. 3** Overall flow chart of the volume calculation algorithm

Volume calculation

$A_{\mathrm{R,l}}(n)$ $A_{\mathrm{R,r}}(n)$	Calculate area of the segmented images
$\bar{x}_{\mathrm{R,l}}(n)$ $\bar{x}_{\mathrm{R,r}}(n)$	Calculate centroid of the area
$V^{\mathrm{out}}(n)$	Calculate volume expanded out from the parallel plates
$V^{\mathrm{in}}(n)$	Calculate volume between the parallel plates
$V(n)$	Calculate nth total volume
$n = n + 1$	

Fig. 4 Detailed algorithm sequence for the volume calculation

Description of the Volume Calculation Algorithm

Figures 3 and 4 illustrate the framework of the proposed algorithm for calculating volumetric changes of the foam. The algorithm consists of four stages: (1) image acquisition, (2) preprocessing, (3) segmentation, and (4) volume calculation.

Image Acquisition

For image acquisition, a 30-min video capturing the changes in each foam sample was recorded during rheological measurements. Each frame of the video had a resolution of 1080 pixels × 1920 pixels (width × height). To compute the volume expansion of each ECP/PBA foam, the recorded video was segmented into a series of frames. Subsequently, the region of interest (ROI) was defined as the region of the ECP/PBA foam extruding from the rheometer geometry. The

ROI $[F_{\mathrm{R}}^n(x, y)]$ was extracted from each frame $[F^n(x, y)]$ and cropped to a size of 3.5 mm × 3.5 mm to expedite computation (Fig. 3b) [21]. Here, the superscript n indicates the frame number.

Given that each frame consists of a series of pixels, we calculated the number of pixels per ROI length (N_{R}) using the following equations:

$$l_{\mathrm{pixel}} = \frac{2R_{\mathrm{geo}}}{\text{Number of pixels per } 2R_{\mathrm{geo}}}, \tag{1}$$

$$N_{\mathrm{R}} = \frac{\text{ROI length} (= 3.5 \text{ mm})}{l_{\mathrm{pixel}}}, \tag{2}$$

where l_{pixel} is the unit length of a pixel and R_{geo} is the radius of the geometry (= 4 mm). For more precise calculations, the left and right sections of the ROI $[F_{\mathrm{R,l}}^n(x, y)$ and $F_{\mathrm{R,r}}^n(x, y)]$ were analyzed separately. Throughout this paper, the subscripts, l and r, indicate the left and right regions of the ROI, respectively. Each segmented frame, $F_{\mathrm{R,l}}^n(x, y)$ and $F_{\mathrm{R,r}}^n(x, y)$, consisted of an $N_{\mathrm{R}} \times N_{\mathrm{R}}$ matrix array.

Preprocessing

Generally, a commercial camera equipped with a complementary metal–oxide–semiconductor (CMOS) sensor produces noisier images under low illumination conditions. As a result, nonuniform illuminance is observed in the images under uneven lighting conditions [22]. Thus, preprocessing must be performed before segmentation and volume calculations. In this study, we used three common preprocessing methods: median filter (P1), equalizing illumination (P2), and contrast stretching (P3). Figure 3c–h illustrate the effects of each method.

Segmentation

To accurately calculate the total volume of each sample, the image of the ECP/PBA region extruding from the parallel plates must be distinguished from the background. Thus, image segmentation was performed using locally adaptive thresholding methods [23, 24]. Figure 3i and j shows the histograms of the pixels consisting of $F_{\mathrm{R,l}}^n(x, y)$ and $F_{\mathrm{R,r}}^n(x, y)$ as functions of image intensity (I). The histograms were fitted using a bimodal Gaussian function $[P(I)]$ of Eq. (3):

$$P(I) = P_{\mathrm{B}}(I) + P_{\mathrm{O}}(I)$$
$$= \frac{P_{\mathrm{B,0}}}{\sqrt{2\pi}\sigma_{\mathrm{B}}} \exp\left[-\frac{(I - \mu_{\mathrm{B}})}{2\sigma_{\mathrm{B}}^2}\right] + \frac{P_{\mathrm{O,0}}}{\sqrt{2\pi}\sigma_{\mathrm{O}}} \exp\left[-\frac{(I - \mu_{\mathrm{O}})}{2\sigma_{\mathrm{O}}^2}\right], \tag{3}$$

where $P_B(I)$ is the Gaussian distribution of the background and $P_O(I)$ is the Gaussian distribution of the object. Thereafter, two threshold values (TS_l and TS_r) for the left- and right-ROI regions were calculated using Eq. (4):

$$TS_l = \max\left\{I|P_{B,l}(I) < 20\right\}, \; TS_r = \max\left\{I|P_{B,r}(I) < 20\right\}.$$ (4)

The segmented images [$S_{R,l}^n(x, y)$ and $S_{R,r}^n(x, y)$] were defined as in Eq. (5):

$$S_{R,l}^n = \begin{cases} 1 \text{ if } F_{R,l}^n(x, y) > TS_l \\ 0 \text{ if } F_{R,l}^n(x, y) \leq TS_l \end{cases}, \; S_{R,r}^n = \begin{cases} 1 \text{ if } F_{R,r}^n(x, y) > TS_r \\ 0 \text{ if } F_{R,r}^n(x, y) \leq TS_r \end{cases},$$ (5)

As a result of the segmentation process, 0 was assigned to the background, while 1 was assigned to the ECP/PBA region extruding from the parallel plates (Fig. 3k and l).

Volume Calculation

As depicted in Fig. 4, the total volume [$V(n)$] of each ECP/PBA compound was computed as the sum of the volume extruding from the parallel plates [$V^{out}(n)$] and the internal volume determined by R_{geo} and the gap size [$V^{in}(n)$]. Notably, $V^{out}(n)$ was calculated based on Pappus's centroid theorem [24, 26]. According to the second theorem of Pappus, the volume of a solid of revolution generated by rotating a surface about an external axis is equal to the product of the surface area and the length of the path traced by the centroid of the surface area. The areas of the segmented images [$A_{R,l}(n)$ and $A_{R,r}(n)$] were calculated as the product of the sum of the array elements and the area of each unit pixel (Eq. (6)):

$$A_{R,l}(n) = \left\{\sum_{x=1}^{N_R}\sum_{y=1}^{N_R} S_{R,l}^n(x, y)\right\} \times \left(l_{pixel}\right)^2,$$
$$A_{R,r}(n) = \left\{\sum_{x=1}^{N_R}\sum_{y=1}^{N_R} S_{R,r}^n(x, y)\right\} \times \left(l_{pixel}\right)^2.$$ (6)

The distance from the centroid of the surface area to the axis of rotation was computed as the sum of R_{geo} and the centroid of each segmented image [$\bar{x}_{R,l}(n)$ and $\bar{x}_{R,r}(n)$]. Since each segmented image comprised a square of pixels, the centroids of individual segmented images could be computed by dividing the images into hypothetical rectangular elements arranged in rows and calculating the centroid and area of each rectangular element. The centroids of individual segmented images were calculated using Eq. (7):

$$\bar{x}_{R,l}(n) = \frac{\left(l_{pixel}/2\right) \cdot \sum_{x=1}^{N_R}\left\{\sum_{y=1}^{N_R} S_{R,l}^n(x, y) \times l_{pixel}\right\}^2}{A_{R,l}(n)},$$
$$\bar{x}_{R,r}(n) = \frac{\left(l_{pixel}/2\right) \cdot \sum_{x=1}^{N_R}\left\{\sum_{y=1}^{N_R} S_{R,r}^n(x, y) \times l_{pixel}\right\}^2}{A_{R,r}(n)}$$ (7)

Then, $V^{out}(n)$ was calculated as the sum of the half volumes of left- and right-ROI regions [Eq. (8)].

$$V^{out}(n) = \frac{\left[2\pi\left\{R_{geo} + \bar{x}_{R,l}(n)\right\} \times A_{R,l}(n)\right]}{2} + \frac{\left[2\pi\left\{R_{geo} + \bar{x}_{R,r}(n)\right\} \times A_{R,r}(n)\right]}{2}.$$ (8)

In addition, $V^{in}(n)$ was calculated using Eq. (9):

$$V^{in}(n) = \pi R_{geo}^2 \times \text{gap}(n),$$ (9)

where gap(n) is the gap size between the parallel plates, which was automatically adjusted to maintain a constant axial normal force. Due to differences in the number of time data points in rheological measurements and the total frame number of $V^{out}(n)$, the piecewise cubic Hermite interpolating polynomial (PCHIP) method was used to match the number of data points [27].

For further analysis of the foaming process, the volume expansion ratio (VER) and cell volume fraction (ϕ_{cell}) were calculated as follows:

$$\text{VER} = \frac{V(n)}{V_0},$$ (10)

$$\phi_{cell}(n) = \phi_{cell,0} + \frac{V(n) - V_0}{V(n)} = \phi_{cell,0} + \left(1 - \frac{1}{\text{VER}}\right),$$ (11)

where V_0 is the volume of the sample in the first frame [$= \pi R_{geo}^2 \cdot \text{gap}(1)$] and $\phi_{cell,0}$ is the initial cell volume fraction.

Results and Discussion

Characterization of Foaming and Curing Process Using Temperature Ramp Tests

Figure 5 presents storage modulus (G'), loss modulus (G''), and tan δ ($= G''/G'$) of ECP as functions of temperature. ECP was used to investigate rheological changes occurring during the curing process without foaming process. ECP displayed typical thermoplastic behavior at low temperatures, where both moduli (G' and G'') decreased continuously. At
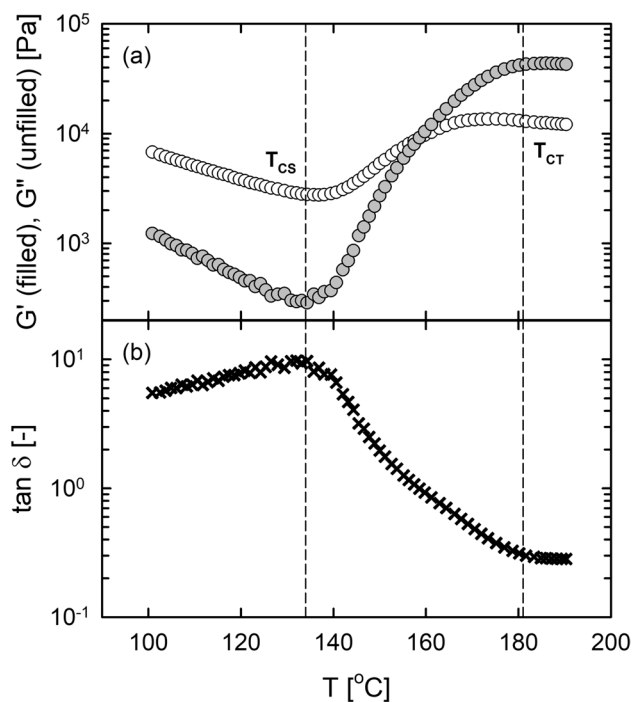
Fig. 5 a Storage (G') and loss (G'') moduli and **b** tan δ of ECP as functions of temperature. T_{CS} and T_{CT} indicate the start and termination of the curing process, respectively

a temperature of 134 °C, the G' value of ECP started to increase and tan δ reached its maximum due to the curing by chemical crosslinking. Thus, the curing start temperature (T_{CS}) of ECP was determined to be 134 °C. The curing reaction was initiated at T_{CS} by the thermal decomposition of DCP. As a result, 2-phenylpropanoxy radicals were generated and then further decomposed into methyl radicals. These methyl radicals abstracted hydrogens atoms from the EOC chains, yielding cross-linked EOC chain radicals [8]. The curing process was deemed complete at the curing termination temperature (T_{CT}) of 181 °C, as evidenced by the plateau of G'.

Figure 6 shows the effects of both foaming and curing processes on the rheological and volumetric changes of ECP/PBA4. The video showing whole volumetric change of the ECP/PBA4 during the temperature ramp test is provided as Supplementary Information. Five distinct temperature regimes were defined based on four critical temperatures: foaming start temperature (T_{FS}), T_{CS}, cell shrinkage temperature (T_{SS}), and T_{CT}.

In the regime I, both moduli (G' and G'') of ECP/PBA4 decreased with increasing temperatures (Fig. 6a). However, the volumetric changes (V^{in} and V^{out}) of its inner and outer regions were negligible (Fig. 6b). Thus, ϕ_{cell} was constant, indicating that foaming and curing did not occur in this
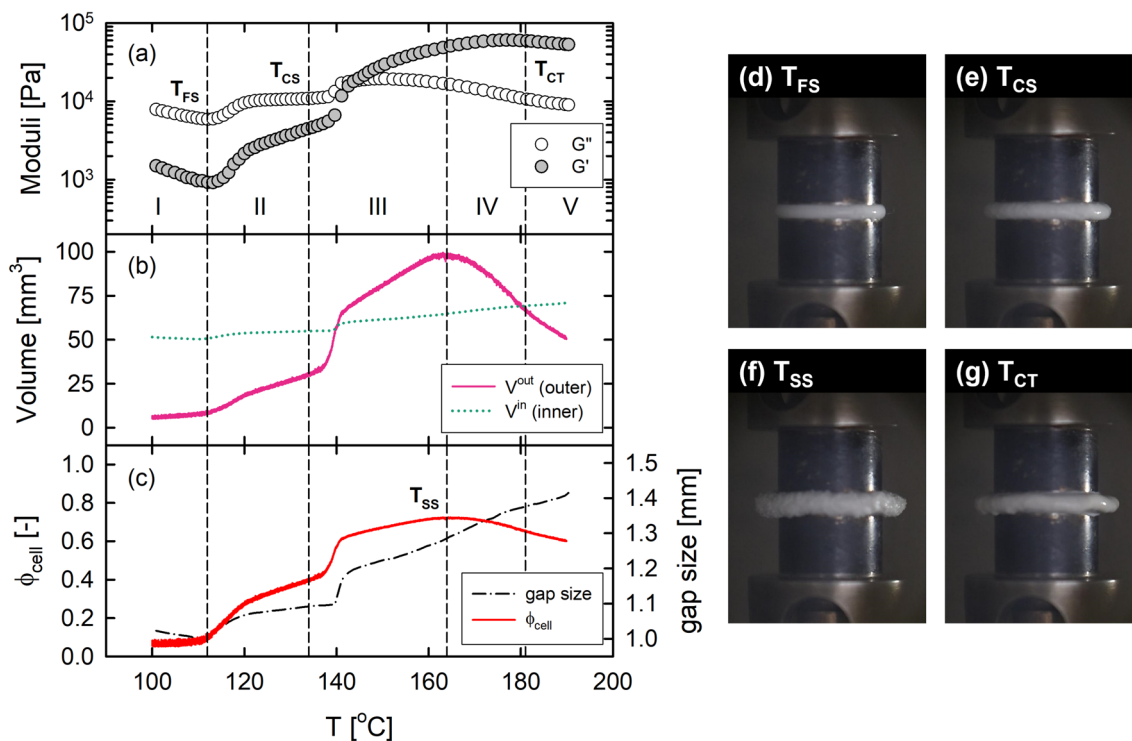

Fig. 6 Rheological and volumetric properties of ECP/PBA4 as functions of temperature: **a** storage (G') and loss (G'') moduli, **b** volumetric changes of the inner (V^{in}) and outer (V^{out}) regions, **c** ϕ_{cell} (left y-axis) and gap size (right y-axis). DSLR camera images of the ECP/ PBA4 captured at four critical temperatures, **d** T_{FS}, **e** T_{CS}, **f** T_{SS}, and **g** T_{CT}. The definitions of the critical temperatures are presented in the main text

temperature regime (Fig. 6c). It is noted that $\phi_{cell,0}$ was not zero due to the presence of unexpanded PBA as micro-sized capsules.

Upon reaching the regime II at 112 °C, the foaming process started. The moduli, volume, ϕ_{cell}, and gap size of ECP/PBA4 increased simultaneously at 112 °C. Thus, the foaming start temperature (T_{FS}) of the ECP/PBA4 was determined to be 112 °C, where the maximum tan δ was observed (Fig. 7b). Interestingly, this T_{FS} value was quite close to the temperature (115 °C) determined by the axial normal force method in our previous study [8].

As described in "Introduction", the encapsulated PBA used contained a low-boiling-point liquid hydrocarbon inside an acrylonitrile copolymer shell. This copolymer shell started softening at T_{FS}. Simultaneously, the hydrocarbon was gasified, increasing the internal pressure [8, 9]. The resulting expanded foam cells acted as microsphere fillers, which enhanced rheological and volumetric properties. The acrylonitrile copolymer shell was in a solid state under experimental conditions without melting, decomposition, or degradation. Therefore, this highly elastic shell significantly increased G' over G''. The expansion force generated by the foaming was compensated by the gap increase and the sample flow out of the geometry. However, the development of ϕ_{cell} during the entire foaming process was primarily attributed to V^{out}, as shown in Fig. 6b.

Intriguingly, the ECP/PBA4 exhibited rapid increments in both V^{out} and ϕ_{cell} near 140 °C. In the regime III, the volumetric properties were affected by both curing

and foaming processes because the moduli of the ECP matrix increased at T_{CS} of 134 °C (Fig. 5a). However, we speculated that the effective curing of ECP/PBA4 occurred below 134 °C. The thermal decomposition of DCP can be initiated at 120 °C [8]. Expanding cells can exert shear forces on the surrounding ECP matrix, which pushes and confines the matrix as the foaming proceeds [9, 28]. Thus, the curing of the ECP/PBA4 was speculated to be activated at lower temperatures. With increasing temperatures, the PBA-containing capsules expanded continuously because the acrylonitrile copolymer shell softened more and vapor pressure of gasified hydrocarbon increased exponentially. Meanwhile, the growth of the foam cells was impeded by the confinement of the hardened matrix and rheometer geometries. The scanning electron microscopy (SEM) images presented in our previous study revealed a compact arrangement of the foam cells at 140 °C [8]. These competing forces resulted in the sudden increases in V^{out} and ϕ_{cell} near 140 °C. Consequently, under the confined environment, the contacts between expanding cells resulted in additional sample flow out from the geometries, leading to an increase in V^{out} beyond V^{in}.

The cell expansion terminated at 164 °C, in which the cell shrinkage temperature (T_{SS}) was defined. In the regime IV, ϕ_{cell} decreased monotonically after peaking at T_{SS}. The gap size continued to increase with the increasing hardening of the ECP matrix. Thus, the observed decrease in ϕ_{cell} solely originated from the shrinkage of the foamed cells. Exposure to such high temperatures led to the permeation of the
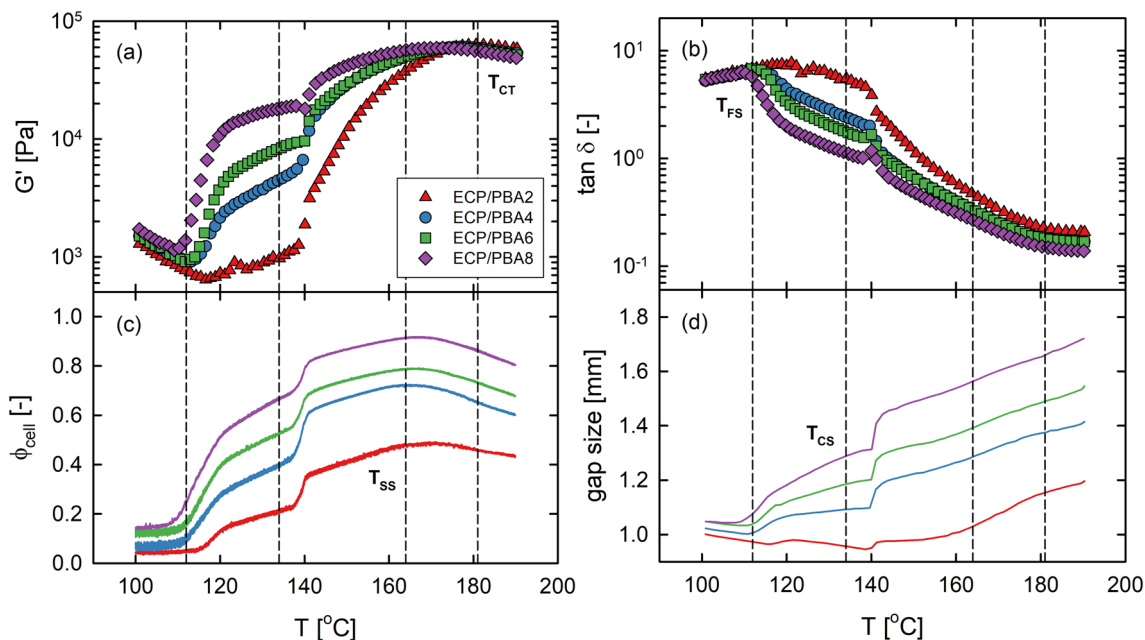

Fig. 7 Rheological parameters and ϕ_{cell} of all ECP/PBA foams at different PBA concentrations (2, 4, 6, and 8 phr). **a** G', **b** tan δ, **c** ϕ_{cell}, and **d** gap size as functions of temperature. Vertical dashed lines indicate the critical temperatures of ECP/PBA4

gasified hydrocarbon through the thin copolymer shell [8]. The G' value of ECP/PBA4 reached its maximum at 177 °C due to a balance between the curing effect (increase in G') and cell shrinkage (decrease in G'). In the regime V, the moduli and volumetric properties of ECP/PBA4 decreased gradually due to cell shrinkage.

The effect of the PBA concentration on rheological parameters and ϕ_{cell} is presented in Fig. 7 and Table 2. Morphological images and analysis at each PBA concentration can be found in our previous study [8]. Figure 7 displays G', tan δ, ϕ_{cell}, gap size of the ECP/PBA foams. Below T_{FS}, the G' of the ECP/PBA foams increased slightly with increasing $\phi_{cell,0}$ due to the weak hydrodynamic effects of unexpanded PBA capsules (Fig. 7a and Table 2). The larger $\phi_{cell,0}$ also reduced T_{FS} (115 °C for 2 phr → 108 °C for 8 phr). The effect of the PBA concentration was more pronounced in the regime II, where G' increased with increasing PBA concentration. Intriguingly, while the gap size at 2 phr of PBA decreased after a small increase of 0.02 mm, an abrupt gap increase of over 0.1 mm was observed at the beginning of the cell expansion for 4, 6, and 8 phr (Fig. 7d). In the regime III, all ECP/PBA foams exhibited the identical behavior in G' and ϕ_{cell}. Near 140 °C, a sharp increase of G' and ϕ_{cell} resulted from the interplay between cell expansion, curing, and geometric confinement. Cell shrinkage occurred averagely at 167 °C, regardless of PBA concentrations (Fig. 7c and Table 2). At T_{SS} of 167 °C, the ϕ_{cell} of all ECP/PBA foams started decreasing from their maximum. However, increasing PBA loadings led to increments in ϕ_{cell} values (Table 2).

Rheological and Volumetric Changes During Hypothetical Process Sequence

To describe time-resolved changes that might occur during an actual foaming process, we used a time–temperature protocol consisting of a series of time sweep and temperature ramp tests, as outlined in Fig. 1. The first stage of the protocol involved a time sweep test at 100 °C ($< T_{FS}$). After 1 min, the temperature increased rapidly (60 °C/min) up to 170 °C. Since 170 °C exceeds T_{FS}, T_{CS}, and T_{SS}, cell expansion, curing, and cell shrinkage occurred sequentially during this heating phase. In the third stage, changes in the rheology and volume expansion ratio (VER) [Eq. (10)] were tracked in the time sweep mode for 10 min. Notably, the first,
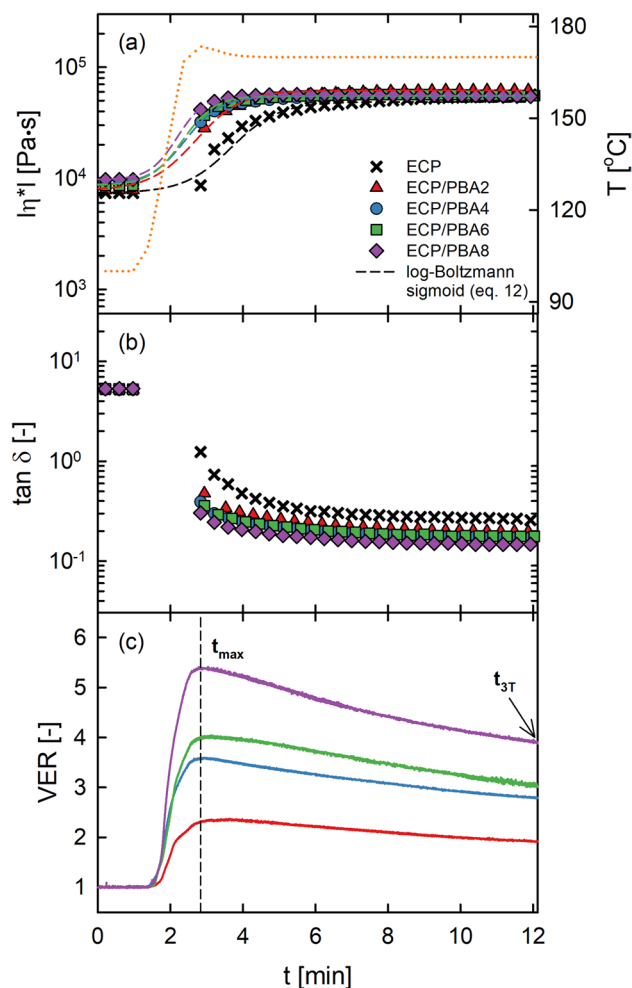

Fig. 8 Rheological properties and VER of the ECP/PBA foams in the first, second, and third stages. **a** |η^*| (left y-axis), **b** tan δ, and **c** VER as functions of time. In **a**, the right y-axis indicates the temperature profile (orange dotted line)

second, and third stages correspond to the heating phase. Finally, in the fourth stage, the temperature was decreased at 10 °C/min to analyze the changes occurring during cooling (cooling phase).

Figure 8 shows the rheological and VER changes of all ECP/PBA foams at 170 °C during heating phase (first, second, and third stages). As expected, the rheological properties and VER were constant at 100 °C. A slight increase in complex viscosity (|η^*|) resulted from the weak

Table 2 Summary of critical temperatures and ϕ_{cell} values of ECP/PBA foams. All ECP/PBA foams had the same T_{CS} and T_{CT} at 134 °C and 181 °C

Name	T_{FS} [°C]	T_{CS} [°C]	T_{SS} [°C]	T_{CT} [°C]	$\phi_{cell,0}$ [−]	ϕ_{cell} at T_{SS} [−]
ECP/PBA2	115	134	169	181	0.04	0.49
ECP/PBA4	111		164		0.08	0.72
ECP/PBA6	110		167		0.11	0.79
ECP/PBA8	108		167		0.14	0.92

Table 3 Fitting parameters obtained from Eq. (12)

Name	η_0 [Pa s]	η_f [Pa s]	t_{inf} [s]	t_{reac} (=4Δt) [s]
ECP	7372	48,754	221	157
ECP/PBA2	7816	61,789	162	151
ECP/PBA4	8718	54,768	144	118
ECP/PBA6	8618	55,455	140	107
ECP/PBA8	9720	55,737	131	91

hydrodynamic effects of the unexpanded PBA capsules. With increasing temperatures, $|\eta*|$ exhibited an S-shaped increase due to the simultaneous occurrence of foaming and curing. For a quantitative description, the behavior of $|\eta*|$ was analyzed using the log-Boltzmann sigmoid equation of Eq. (12) [29–31]:

$$\log|\eta*|(t) = \log\eta_f + \frac{\log\eta_0 - \log\eta_f}{1 + e^{(t-t_{inf})/\Delta t}}, \quad (12)$$

where η_0 is the initial viscosity, η_f is the final viscosity, t_{inf} is the inflection time, and Δt is the time constant for the curvature transition rate. At t_{inf}, the sample viscosity is halfway between $\log\eta_0$ and $\log\eta_f$. The slope of the sigmoid curve at t_{inf} can be calculated using the following equation:

$$\left.\frac{d\log|\eta*|}{dt}\right|_{t=t_0} = \frac{\log\eta_f - \log\eta_0}{4\Delta t}. \quad (13)$$

In Eq. (13), the $4\Delta t$ can be used to interpret the reaction time taken for foaming and curing. Thus, the total reaction time (t_{reac}) was defined as $4\Delta t$, which represents the time required for the transition from $\log\eta_0$ to $\log\eta_f$. The corresponding fitting parameters are listed in Table 3. The reaction by only curing was complete after 157 s. Interestingly, t_{reac} was accelerated by the simultaneous occurrence of foaming and curing. Adding 2 phr of PBA slightly decreased t_{reac} by 6 s. However, PBA concentration exceeding 4 phr lowered t_{reac} by more than 40 s.

The volume expansion resulting from cell expansion and curing started immediately after the temperature reached approximately 120 °C (~ 1.5 min). As the temperature approached T_{SS}, maximum VER was consistently observed at 2.83 min (= t_{max}) regardless of PBA concentrations. As expected, the maximum VER values of the samples increased with increasing PBA concentrations. Afterwards, the VER decreased gradually due to cell shrinkage resulting from gas permeation through the shell. Conversely, $|\eta*|$ remained almost constant.

Figure 9 presents the rheological and VER changes of ECP/PBA foams at 170 °C during the cooling phase (fourth stage). As evidenced in Fig. 9c, cell shrinkage
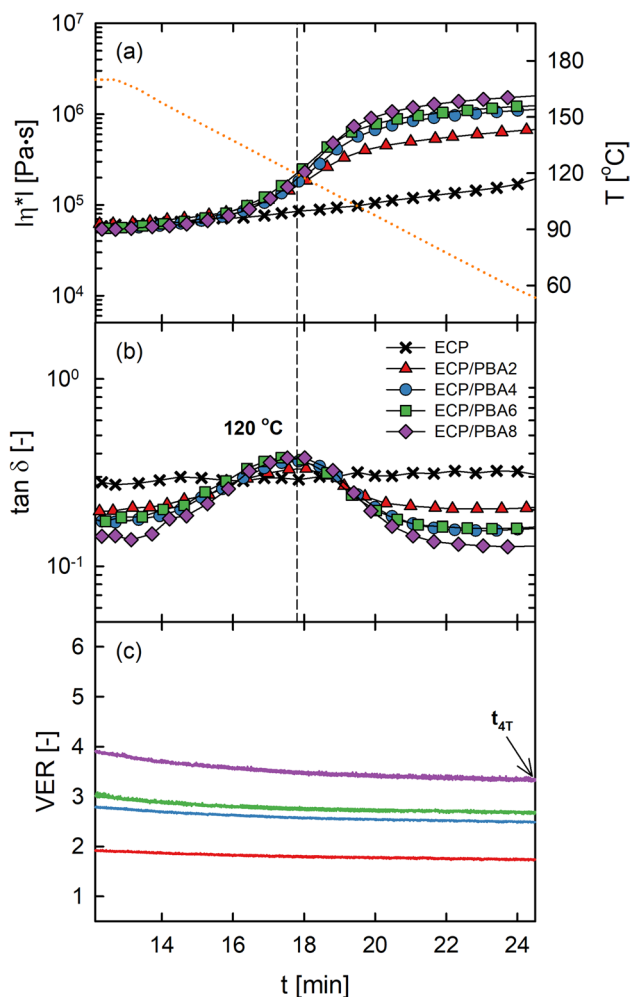

Fig. 9 Rheological properties and VER of all ECP/PBA foams in the fourth stage. **a** $|\eta*|$ (left *y*-axis), **b** tan δ, and **c** VER as functions of time. In **a**, the right *y*-axis indicates the temperature profile (orange dotted line)

occurred during this cooling phase. However, on the contrary to the third stage, the primary cause of the cell shrinkage in the fourth stage was the reduction in the internal gas pressure resulting from decreasing temperatures. The rheological properties exhibited no significant changes from 170 to 150 °C (Fig. 9a and b). Meanwhile, the $|\eta*|$ and tan δ of the ECP/PBA foams started to increase below 150 °C (~ 14.4 min). Moreover, peaks in the tan δ curves were observed at 120 °C, corresponding to the start temperature of volume expansion in the second stage. Since the tan δ of ECP without the PBA was almost independent of temperature (Fig. 9b), it was reasonable to assume that the tan δ peaks observed for the ECP/PBA foams originated from the properties of the encapsulated PBA. We attributed these peaks to transition between the softening and hardening of the acrylonitrile copolymer shell, akin

to the glass transition of amorphous polymers. However, it was difficult to figure out the details because the information on copolymer components was not known.

For a quantitative comparison of the extent of cell shrinkage during the third and fourth stages, two shrinkage factors (S_3 and S_4) were defined as follows:

$$S_3 = \frac{V(t_{max}) - V(t_{3T})}{V(t_{max})} \times 100\%, \tag{14}$$

$$S_4 = \frac{V(t_{3T}) - V(t_{4T})}{V(t_{3T})} \times 100\%, \tag{15}$$

where t_{3T} and t_{4T} are the termination times of the third and fourth stages, respectively. The two shrinkage factors (S_3 and S_4) as functions of PBA concentrations are shown in Fig. 10. As depicted, S_3 was approximately twice that of S_4, indicating that the cell shrinkage resulting from gas permeation at high temperatures was more significant than that resulting from reduced internal gas pressures.

Finally, to validate our volume calculation algorithm, we measured the actual densities of all ECP/PBA foams (ρ_{mea}) and compared them with their corresponding calculated densities (ρ_{cal}). For this, each ECP/PBA compound was weighed before rheological measurements, and ρ_{cal} was calculated based on the volume obtained from the algorithm of Figs. 3 and 4. After the measurements, the ρ_{mea} of each ECP/PBA foam was experimentally measured using a densimeter (MD-300S, Alfa Mirage, Japan) at room temperature. Figure 11 plots two densities as the abscissa and ordinate. The two densities coincided well with each other ($R^2 = 0.994$). In addition, we calculated error factors (ε_f) using the following equation:

Fig. 10 Shrinkage factors (S_3 and S_4) of all ECP/PBA foams as functions of PBA concentrations at the end of the third and fourth stages, respectively
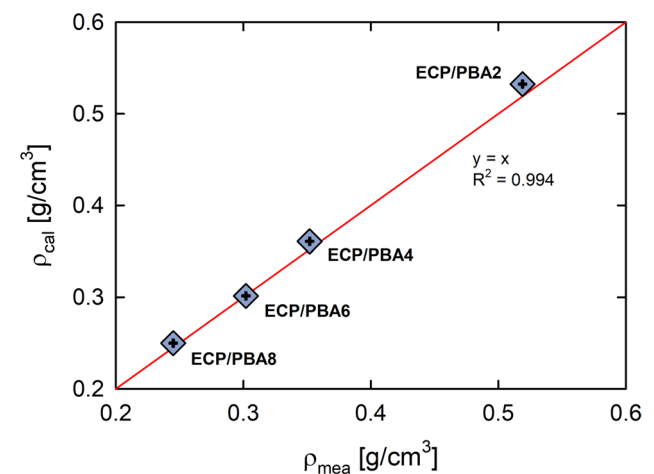
Fig. 11 Comparison between the densities calculated using the volume calculation algorithm (ρ_{cal}) and the those measured using a densimeter (ρ_{mea})

$$\varepsilon_f = \frac{|\rho_{cal} - \rho_{mea}|}{\rho_{cal}} \times 100\%. \tag{16}$$

Table 4 lists the resulting error factors, which are below 3% for all ECP/PBA foams. Thus, these results confirmed the validity of the volume calculation algorithm adopted in this study.

Conclusions

To simultaneously capture the rheological and volumetric changes occurring during the foaming and curing of a TPE containing an encapsulated PBA, we combined the conventional rotational rheometer with a commercial digital camera. During rheological measurements, the digital camera recorded a video depicting volumetric changes under specified temperature conditions. Subsequently, a computational algorithm based on computer vision was used to digitize the recorded video images into quantitative volume data.

Four critical temperatures (T_{FS}, T_{CS}, T_{SS}, and T_{CT}) were identified from the temperature ramp tests in the range of 100 °C and 190 °C. At each critical temperature, foaming and curing led to structural changes in the TPE foam,
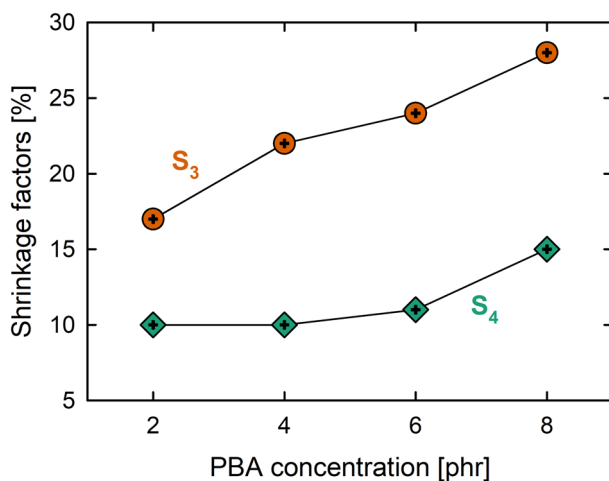
Table 4 Summary of the foam densities (ρ_{cal} and ρ_{mea}) and error factors (ε_f) at 170 °C

	c_{all} [g/cm^3]	ρ_{mea} [g/cm^3]	ε_f [%]
ECP/PBA2	0.532	0.519	2.516
ECP/PBA4	0.361	0.352	2.410
ECP/PBA6	0.301	0.302	0.188
ECP/PBA8	0.250	0.245	1.978

resulting in corresponding rheological and volumetric changes. Specifically, the shear moduli increased in the regimes II and III (Fig. 6) with increments in ϕ_{cell} during cell expansion. After T_{SS} of 167 °C, ϕ_{cell} started to decrease due to cell shrinkage, regardless of the PBA concentrations (2, 4, 6, and 8 phr). However, the larger maximum ϕ_{cell} was definitely obtained at higher PBA concentrations. As a result of decreasing ϕ_{cell}, the shear moduli also gradually decreased. Thus, the effects of cell expansion and shrinkage were successfully captured using the camera-equipped rheometer setup and the proposed algorithm.

In addition, we designed a four-stage time–temperature protocol based on the above critical temperatures, which mimicked the changes induced by cell expansion and shrinkage during an actual foaming process. As the temperature increased rapidly from 100 to 170 °C, the foam volume increased considerably until its maximum at 170 °C. Afterwards, as the temperature approached T_{SS} in the third stage and the internal pressure of cells decreased in the fourth stage, the foam volume reduced gradually. When volume reduction degrees across stages were compared, the volume change in the third stage was averagely twofold that in the fourth stage. After the application of the four-stage protocol, the density of the obtained foam was measured using a densimeter to confirm that our algorithm captured the volumetric changes in a fully quantitative manner. The results revealed that the density computed by the algorithm closely matched the measured density, validating of the suggested algorithm.

The image processing algorithm introduced in this study is not limited to specific material systems and is thus expected to be applicable for investigating the volumetric changes of any type of foam. One promising application is the 3D printing of polymer foams, wherein products are manufactured through layer-by-layer extrusion and stacking of foams. For the commercialization of foam 3D printing, precise volume control is essential to prevent excessive product-shape changes during foam expansion [5–7]. In this regard, our algorithm can be utilized to optimize foam-processing conditions.

Declarations

Conflict of Interest The authors declare no conflict of interest.

References

1. S.-T. Lee, N.S. Ramesh, *Polymeric Foams: Mechanisms and Materials*, 1st edn. (CRC Press, Boca Raton, 2004)
2. S.-T. Lee, *Polymeric Foams: Innovations in Technologies and Environmentally Friendly Materials*, 1st edn. (CRC Press, Boca Raton, 2022)
3. D. Eaves, *Handbook of Polymer Foams*, 1st edn. (iSmithers Rapra Publishing, Shrewsbury, 2004)
4. Y. Mao, R. Qi, J. Appl. Polym. Sci. **109**, 3249 (2008)
5. M. Nofar, J. Utz, N. Geis, V. Altstädt, H. Ruckdäschel, Adv. Sci. **9**, 2105701 (2022)
6. K. Kalia, B. Francoeur, A. Amirkhizi, A. Ameli, A.C.S. Appl, Mater. Interfaces **14**, 22454 (2022)
7. A. Pawar, G. Ausias, Y.-M. Corre, Y. Grohens, J. Férec, Addit. Manuf. **58**, 103066 (2022)
8. H.J. Kong, S.H. Lee, D.G. Kim, H.J. Kim, G.W. Park, K. Hyun, J. Appl. Polym. Sci. **136**, 47358 (2019)
9. S.H. Lee, H.Y. Song, D.G. Kim, S.W. Lim, E.Y. Park, K. Hyun, Macromol. Res. **25**, 325 (2017)
10. R. Liao, W. Yu, C. Zhou, Polymer **51**, 568 (2010)
11. R. Liao, W. Yu, C. Zhou, Polymer **51**, 6334 (2010)
12. M. Abbasi, L. Faust, M. Wilhelm, Polymer **193**, 122351 (2020)
13. M. Abbasi, L. Faust, M. Wilhelm, Polymer **193**, 122354 (2020)
14. B. Jähne, H. Haussecker, P. Geissler, *Handbook of Computer Vision and Applications*, 1st edn. (Princeton, Citeseer, 1999)
15. D. Kim, J. Choi, J. Nam, Meas. Sci. Technol. **26**, 125601 (2015)
16. D. Kim, J. Choi, J. Nam, J. Microsc. **262**, 274 (2016)
17. A.F. Goldszal, C. Davatzikos, D.L. Pham, M.X.H. Yan, R.N. Bryan, S.M. Resnick, J. Comput. Assist. Tomogr. **22**, 827 (1998)
18. I.-B. Lee, S.-H. Min, D.-G. Seo, Dent. Mater. **28**, 212 (2012)
19. D.W. Shattuck, S.R. Sandor-Leahy, K.A. Schaper, D.A. Rottenberg, R.M. Leahy, Neuroimage **13**, 856 (2001)
20. C.D. Barry, C.P. Allott, N.W. John, P.M. Mellor, P.A. Arundel, D.S. Thomson, J.C. Waterton, Ultrasound Med. Biol. **23**, 1209 (1997)
21. R. Boellaard, N.C. Krak, O.S. Hoekstra, A.A. Lammertsma, J. Nucl. Med. **45**, 1519 (2004)
22. P. Korkmaz, B.E. Akgul, K.V. Palem, L.N. Chakrapani, Jpn. J. Appl. Phys. **45**, 3307 (2006)
23. H. Liu, K.C. Jezek, Int. J. Remote Sens. **25**, 937 (2004)
24. P. Moallem, N. Razmjooy, J. Appl. Res. Technol. **10**, 703 (2012)
25. A.W. Goodman, G. Goodman, Am. Math. Mon. **76**, 355 (1969)
26. D. Zwillinger, *CRC Standard Mathematical Tables and Formulas, edn* (CRC Press, Boca Raton, 2018)
27. F.N. Fritsch, R.E. Carlson, SIAM J. Numer. Anal. **17**, 238 (1980)
28. S.A. Khan, J. Rheol. **36**, 573 (1992)
29. B.J. Love, F.P. Ruinet, F. Teyssandier, J. Polym. Sci. Part B Polym. Phys. **46**, 2319 (2008)
30. B.J. Love, F. Teyssandier, Y.Y. Sun, C.P. Wong, Macromol. Mater. Eng. **293**, 832 (2008)
31. N.A.K. Meznarich, B.J. Love, Macromolecules **44**, 3548 (2011)